Elastic full-waveform inversion of 4C ocean-bottom seismic data: Model parameterization analysis

Jian Cao, Romain Brossier, Ludovic Métivier

Elastic full-waveform inversion of 4C ocean-bottom seismic data: model parameterization analysis

Jian Cao[1*], *Romain Brossier*[1], *Ludovic Métivier*[1,2]

[1] *Univ. Grenoble Alpes, ISTerre, F-38058 Grenoble, France*
[2] *CNRS, Univ. Grenoble Alpes, LJK, F-38058 Grenoble, France*

SUMMARY

Full waveform inversion (FWI), as an efficient seismic imaging tool, is widely used in the investigation of the structure of the Earth. For the oil & gas industry, in addition to the subsurface image, a quantitative estimation of elastic properties from seismic data is crucial for the geophysical characterization and monitoring of the subsurface lithology and reservoirs. In marine surveys, with the emergence of the four-component (4C) ocean-bottom acquisition systems (deploying 1C hydrophone plus 3C geophone on the seabed), more elastic wave propagation effects can be recorded in the seismic data for an elastic property estimation of the subsurface, i.e. extracting medium shear modulus from the S-wave velocity model. Multi-parameter elastic FWI offers the possibility to reconstruct the P-wave (V_p) and S-wave velocity (V_s) models jointly. However, compared with the mono-parameter acoustic FWI, the multi-parameter elastic FWI can be more vulnerable due to the parameter coupling, wave modes conversion and interference. For the purpose of building a robust multi-parameter elastic inversion of the 4C seismic data, we consider a workflow design from the aspect of model parameterization analysis. Three different elastic model parameterizations, $\mathbf{m}_1 = (V_p, V_s)$, $\mathbf{m}_2 = (V_p, V_p/V_s)$ and $\mathbf{m}_3 = (V_p, \sigma)$ (σ is the Poisson's ratio), are analysed in terms of data sensitivity and model gradient feature. Together with synthetic case studies on a series of overburden models with increasing elastic effects and a realistic geological model, we conclude that a workflow of first inverting hydrophone data with (V_p, V_p/V_s) parameterization and then 3C geophone data with (V_p, V_s) parameterization contributes to a robust and reliable V_p and V_s model reconstruction.

INTRODUCTION

During the last few decades, FWI based on the acoustic approximation has achieved the success in deriving P-wave velocity models to obtain accurate and high-resolution images of the subsurface, especially in marine surveys (Sirgue et al., 2010; Morgan et al., 2013; Operto et al., 2015; Kamath et al., 2021). It is because the acoustic approximation holds for the kinematics, and hydrophone or vertical component data are typically dominated by unconverted P-waves (Barnes and Charara, 2009). However, in certain geological scenarios, the presence of strong elastic effects would make the conventional acoustic approximated FWI fail in the accurate velocity model reconstruction. For example, in the regions of salt bodies, the ultrasonic measurements and log data analysis in the Gulf of Mexico reveal that the V_p/V_s ratio of rock salt is less than 2 (Zong et al., 2015), and also in the regions of gas clouds, Poisson's ratio of gas saturated sands lies between 0 and 0.25 indicated by the laboratory data (Jain et al., 2012), which are both far away from the acoustic approximation. In addition, geophysical characterization and monitoring of the subsurface lithology and reservoirs in the oil & gas industry require quantitative estimations of the subsurface elastic properties. The ratio of P-wave velocity to S-wave velocity (V_p/V_s ratio) is a commonly used medium parameter for identifying fluid type (water, oil and gas) and estimating porosity and saturation in hydrocarbon reservoirs, with the help of empirical formulas (Hamada, 2004). Those measurements are of great interest to identify different reservoirs and monitor fluid movements and CO_2 sequestration in time-lapse seismic applications (Liu et al., 2001).

With the emergence of the 4C ocean-bottom seismic acquisition systems, elastic effects can be easily captured through the direct recording of S waves by 3C geophones on the seabed, especially in the horizontal components. To access those elastodynamics information in such data, the FWI based on the elastic wave equation is required, and consequently leads to a multi-parameter inversion problem, in which models of P-wave and S-wave velocity need to be reconstructed jointly. Compared with the mono-parameter acoustic FWI, the strong nonlinearity and parameter trade-offs in multi-parameter elastic FWI make a suitable data- and model-driven workflow design become necessary (Sears et al., 2010; Prieux et al., 2013; Wang et al., 2021). To address this issue, we consider to design a hierarchical FWI workflow from the aspect of model parameterization analysis, so as to choose the appropriate model-parameter set that matches the wave mode dominance in the 4C ocean-bottom data. In the following sections, we first briefly review a 3D fluid-solid coupled elastic FWI engine that can efficiently model and invert the 4C ocean-bottom data (Cao et al., 2022). Then, we derive the model gradients corresponding to three different model parameterizations and analyse their data sensitivity and gradient feature for a hierarchical inversion workflow building. Finally, two synthetic case studies are presented to illustrate the feasibility and robustness of the proposed inversion workflow.

3D FLUID-SOLID COUPLED ELASTIC FWI

Accurate simulations of seismic wave propagation in marine environments can be achieved by solving an acoustic-elastic coupled wave-equation system (Cao et al., 2022), in which the elastic modelling is only required for the subsurface domain while keeping the acoustic modelling in the water layer. The synthetic 4C seismic data are obtained by extracting the wavefields at the seabed, containing the pressure wavefield (P) from the water side and 3C particle displacement ($\mathbf{u}_s$) from the solid side. Base the above forward problem, we define the FWI misfit function of 4C seismic data as

$$J(\mathbf{m}) = \frac{1}{2}\sum\nolimits_{shots}\left(\lambda\|\mathbf{d}_P^{syn}(\mathbf{m}) - \mathbf{d}_P^{obs}\|^2 + (1-\lambda)\|\mathbf{d}_\mathbf{u}^{syn}(\mathbf{m}) - \mathbf{d}_\mathbf{u}^{obs}\|^2\right), \tag{1}$$

where $\mathbf{m}$ denotes the set of model parameters of the subsurface, $\mathbf{d}_P^{obs}$ and $\mathbf{d}_\mathbf{u}^{obs}$ are observed hydrophone and 3C geophone data, respectively, and $\mathbf{d}_P^{syn}$ and $\mathbf{d}_\mathbf{u}^{syn}$ are corresponding synthetic pressure and 3C displacement wavefields at the seabed mentioned above. The scalar λ is a variable that only takes the value of 0 or 1 to indicate which data type is applied during the inversion.

The minimization of $J(\mathbf{m})$ can be solved by local optimization method, more precisely a quasi-Newton l-BFGS method, with an iterative scheme

$$\mathbf{m}_{k+1} = \mathbf{m}_k + \alpha_k \Delta\mathbf{m}_k, \tag{2}$$

where $\alpha_k \in \mathbb{R}^+$ is the step length and the model perturbation

$$\Delta\mathbf{m}_k = -\mathbf{Q}_k \nabla J(\mathbf{m}_k), \mathbf{Q}_k \simeq \left(\nabla^2 J(\mathbf{m}_k)\right)^{-1}, \tag{3}$$

which requires access to the gradient of $J(\mathbf{m})$ obtained from the zero-lag correlation of the incident and adjoint wavefields (Plessix, 2006).

MODEL PARAMETERIZATION ANALYSIS

Compared with the mono-parameter problem, the multi-parameter FWI suffers from trade-offs between parameters and different data sensitivity over wave modes, which would affect the success of recovering each parameter (Operto et al., 2013; Oh and Min, 2017). A numerical radiation patterns computing of the modulus of partial derivative wavefields, with one parameter perturbation point in the model center and the other parameter keeping fixed at the background value, is a good tool to provide intuitive analyses of data sensitivity and interparameter trade-offs. As shown in Figure 1, the radiation patterns of three different model parameterizations ($\mathbf{m}_1 = (V_p, V_s)$, $\mathbf{m}_2 = (V_p, V_p/V_s)$ and $\mathbf{m}_3 = (V_p, \sigma)$) are illustrated, in which variations of the computed modulus in different diffraction modes (P-P, P-S, S-P and S-S) reveal how to infer a specific model parameter from different data. For the commonly used model parameterization of seismic velocity (V_p, V_s), we can observe the V_p model reconstruction only relies on P-P diffracted waves (Figure 1a), which is the same as in the acoustic FWI (Operto et al., 2013). It interprets the applicability of acoustic FWI in achieving a successful V_p model reconstruction, when the data have a

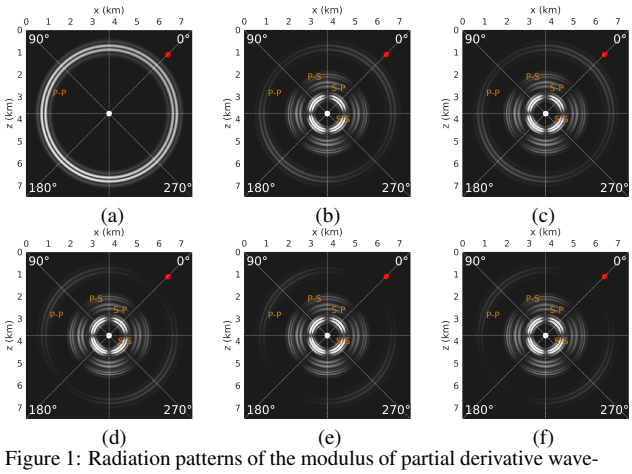

Figure 1: Radiation patterns of the modulus of partial derivative wavefields with respect to (V_p, V_s), (V_p, σ) and $(V_p, V_p/V_s)$ parameterizations. Computed V_p parameter perturbation with fixed V_s (a), σ (b) and V_p/V_s (c), respectively; computed parameter perturbations of V_s (d), σ (e) and V_p/V_s (f) with fixed V_p. The red and white dots denote the incident source and the parameter perturbation point, respectively.

relatively weak elastic-effect imprint or the elastic effects can be mitigated by a data pre-processing (Agudo et al., 2020). The radiation patterns of the other two parameterizations show additional S-related wave modes are involved in the V_p reconstruction (Figures 1b and 1c). From the interparameter trade-off point of view, these two parameterizations make the overlapping of radiation patterns over a broad range of scattering angles, which creates ambiguity in recovering each parameter. However, when considering the inversion of hydrophone data including strong converted P-waves, the introduce of S-related wave modes in the V_p reconstruction provides the possibility of a correct interpretation of P-to-S-to-P converted waves, so as to avoid treating them as P-P reflected waves from wrong reflectors. For the V_s-related model parameters, the same radiation patterns of V_s, V_p/V_s and σ can be observed in Figures 1d-1f, revealing the same data sensitivity in terms of wave modes and scattering angles among them.

In addition, it is also worth analysing the FWI gradient features for different parameters, since it has a direct impact on the model perturbation as shown in Eq. (3). The FWI gradient for parameters V_p/V_s and σ can be derived by applying the chain rule based on the gradients for V_p and V_s,

$$\frac{\partial J(\mathbf{m})}{\partial R} = V_s \left(\frac{\partial J(\mathbf{m})}{\partial V_p} - \frac{\partial J(\mathbf{m})}{\partial V_s} \frac{1}{R} \right), \tag{4}$$

$$\frac{\partial J(\mathbf{m})}{\partial \sigma} = V_s \left(\frac{\partial J(\mathbf{m})}{\partial V_p} - \frac{\partial J(\mathbf{m})}{\partial V_s} \frac{1}{R} \right) / \left(4\sqrt{\frac{1-\sigma}{0.5-\sigma}}(0.5-\sigma)^2 \right), \tag{5}$$

where $R = V_p/V_s$, and $\frac{\partial J(\mathbf{m})}{\partial V_p}$ and $\frac{\partial J(\mathbf{m})}{\partial V_s}$ are gradients for V_p and V_s, respectively. Those two expressions reveal that the V_p gradient would play an important role in their gradient computation, because the scaling factor of the V_p gradient is larger than the one for the V_s gradient. Although it has a negative influence on an isolated V_s reconstruction, the binding effect from the V_p gradient contributes to the stabilization of V_s reconstruction when there is no/relatively weak S-waves can be used in the data, such as inverting the hydrophone data.

To take the benefits of data sensitivity and gradient features in different parameterizations, we propose a two-step hierarchical workflow in the elastic FWI of 4C seismic data:

Step 1: Focus on the V_p reconstruction by inverting hydrophone data with (V_p, R) or (V_p, σ) parameterization, to benefit from additional constraints from converted P-to-S-to-P waves and stabilize the parameter reconstruction of R or σ with the dominated P-waves;

Step 2: Focus on the V_s reconstruction by inverting 3C geophone data with (V_p, V_s) parameterization, with the obtained V_p and V_s models from Step 1 as starting models, to benefit from the weak interparameter trade-off between V_p and V_s in this parameterization and the reliable information of S-waves recorded directly on the seabed.

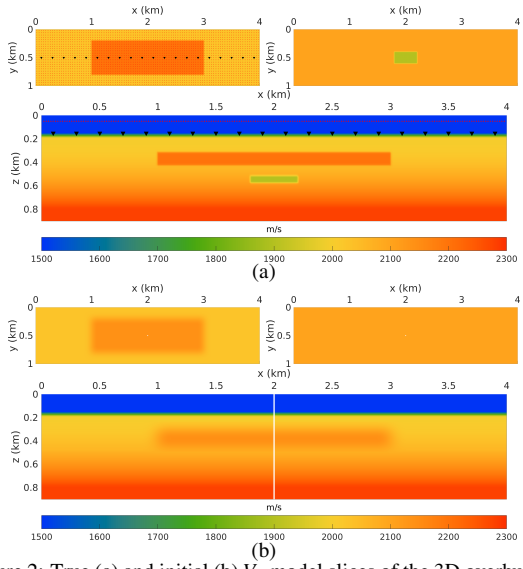

Figure 2: True (a) and initial (b) V_p model slices of the 3D overburden model. The horizontal distribution of shots (red dots) and OBNs (black triangles) are depicted in (a). The well location for extracting velocity profile is indicated in white.

NUMERICAL EXAMPLES

Here, we present two synthetic case studies for the feasibility and robustness evaluation of the proposed two-step hierarchical workflow.

The first case study aims at the robustness test of the workflow in the presence of elastic effects from weak to strong. As shown in Figure 2a, we design a 3D overburden model which contains a high-velocity layer overlying a low-velocity small-scale anomaly. This configuration mimics the hydrocarbon reservoir detection in the subsalt environment. To produce elastic effects with different strength in such model, we change the value of Poisson's ratio σ in the high-velocity overburden from 0.45 to 0.25 and create corresponding S-wave velocity models M_1 to M_5. Note that $\sigma = 0.25$ is usually the rock property of salt bodies. For the other regions, a constant $\sigma = 0.45$ is used to build a more natural soft-seabed environment.

During the test, the observed data for all the models $M_1 - M_5$ are generated by using the fluid-solid coupled modelling solver with a 5 Hz Ricker wavelet source-time function and constant density. The recording system is the ocean-bottom node (OBN) acquisition with 20 4C receiver nodes and 25 shooting lines at 5 m water depth (Figure 2a). We conduct the two-step hierarchical elastic FWI workflow over all the observed data with the same initial models (Figure 2b for V_p and constructed V_s with a constant $\sigma = 0.45$) and inversion parameters (l-BFGS optimization with 30 iterations per step). The resulting V_p and V_s reconstruction results for models $M_1 - M_5$ at each stage are illustrated in Figure 3 in a vertical profile way to give an intuitive view of the workflow robustness with respect to the elastic-effect strength. It can be found that a successful V_p reconstruction is achieved at Stage 1 for all the models (Figure 3a) with (V_p, σ) or (V_p, R) parameterization, while the inversion with (V_p, V_s) parameterization produces a bias with the elastic effect increasing as indicated by black arrows. For clarity, we provide the crossline sections of the reconstructed V_p and V_s for the strong elastic-effect model M_5 in Figure 4. In such case, the reconstructed V_p model shows a thickness reducing of the high-velocity overburden (Figure 4a). The reason could be that the energy of P-to-S-to-P converted waves can be competitive with the reflected P-waves at the presence of strong elastic effects, which would make the P-to-S-to-P converted wave from the overburden top edge interpreted as a $P-P$ reflection from the overburden bottom edge in the (V_p, V_s) parameterization (due to lacking of S-wave related radiation modes), and consequently a wrong reflector close to the overburden top edge is created. The V_s reconstruction from different parameterizations at Stage 1 is mainly influenced by the gradient expression since their radiation patterns are identical as analysed before. As shown in Figures 4f and 4j, thanks to the involving of V_p gradient term in the (V_p, σ) and

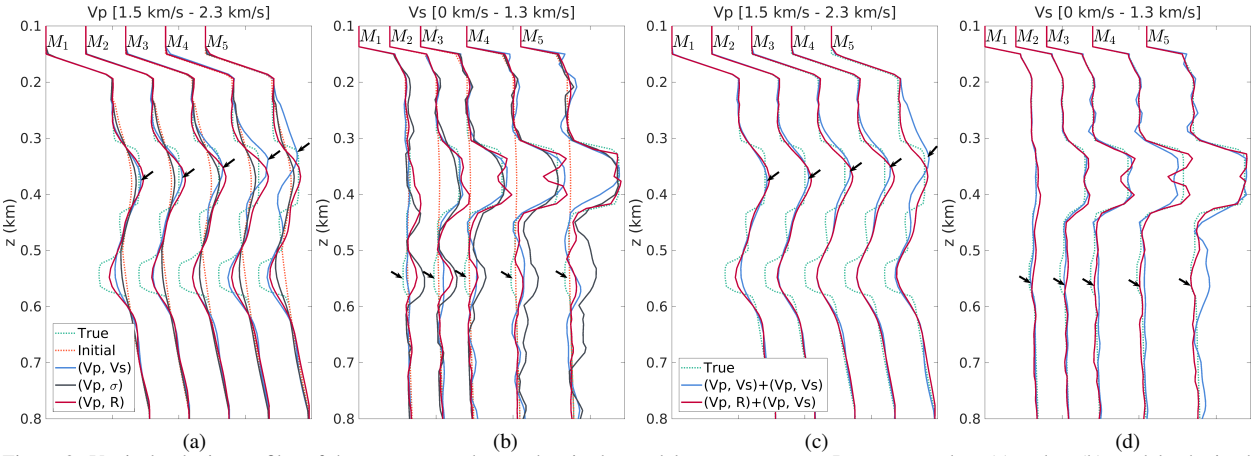

Figure 3: Vertical velocity profiles of the reconstructed V_p and V_s in the model cases M_1 to M_5. Reconstructed V_p (a) and V_s (b) models obtained by inverting hydrophone data with (V_p, V_s), (V_p, σ) and (V_p, R) parameterizations, and reconstructed V_p (c) and V_s (d) models obtained by inverting 3C geophone data with (V_p, V_s) parameterization and the updated V_p and V_s models from (a) and (b). High- and low-velocity anomalies are both highlighted by black arrows.

(V_p, R) parameterizations, their reconstructed V_s models exhibit a low-wavenumber compensation effect from the P-waves, which contributes to stabilizing the inversion. However, the non-linear σ scaling in the σ gradient makes its V_s model suffer from instability issues in the small σ area (Figures 3b and 4j), and that is the reason why we are not going to consider it in the next step. Benefiting from the dominance of S-waves in the 3C geophone data and a good separation between P- and S-wave modes in the (V_p, V_s) parameterization, the V_s model is mainly updated compared with the V_p model at Stage 2 (Figures 3c and 3d), and therefore the V_p bias of the overburden produced by the (V_p, V_s) parameterization in strong elastic-effect scenarios is not mitigated. Consequently, this inaccurate V_p model also influences the correct recovering of the low-velocity anomaly below (Figures 4d). In contrast, the workflow combining (V_p, R) and (V_p, V_s) parameterizations can get an accurate V_p and V_s model reconstruction even in the presence of strong elastic effects (Figures 4g and 4h), revealing its robustness and reliability in both weak and strong elastic-effect scenarios.

In the second case study, we move onto a realistic geological model in the Valhall field. The crossline sections of true V_p, V_s and density models are illustrated in Figures 5a-5c, in which the main inversion challenge is the gas cloud with strong elastic effects (extremely low Poisson's ratio $\sigma = 0.125$). Again, the fluid-solid coupled modelling solver is used to generate the observed 4C data with a 5 Hz Ricker wavelet source time function and OBN acquisition (19 4C receiver nodes and 16 shooting lines at 5 m water depth), and the water free-surface boundary condition is applied in this test. During the FWI, we remove the frequency content less than 2.5 Hz in the observed data and estimate the source wavelet from the data based on the initial models (Figures 5d-5f). To focus on the velocity reconstruction, there is no density update during the FWI iteration. For this study, we consider applying three different two-step workflows to the observed data.

Workflow 1: first perform acoustic FWI on unconverted P-waves (mute Scholte wave and P-to-S-to-P converted wave in the hydrophone data) for a V_p reconstruction, and then use the updated V_p and initial V_s in Figure 5e to invert 3C geophone data by elastic FWI with (V_p, V_s) parameterization for a simultaneous V_p and V_s reconstruction;

Workflow 2: perform elastic FWI with (V_p, V_s) parameterization on the hydrophone data and 3C geophone data in a cascade manner;

Workflow 3: the proposed one of first inverting hydrophone data with (V_p, R) parameterization and then 3C geophone data with (V_p, V_s) parameterization.

Note that, for a better V_s reconstruction, a data pre-processing of Scholte-wave muting and data weighting with respect to the source-receiver offset is applied on the 3C geophone data used for all three workflows to increase the data energy at the intermediate-to-long offset which is dominated by converted P-to-S waves.

The resulting reconstruction of V_p and V_s models from those three workflows are compared in Figure 6. Here we show the V_p models recovered at Stage 1 and the V_s models recovered at Stage 2, which corresponds to the inversion target from the hydrophone data and 3C geophone data. Figure 5a reveals the applicability of acoustic FWI on the uncovered P-wave dominated data, in which the recovered V_p holds for the correct kinematics but suffers from oscillating artifacts along the wave path due to the wrong predicted amplitudes. In addition, because of the lacking of V_s model update from Stage 1 in Workflow 1, a direct use of initial V_s makes the V_s reconstruction cycle skipped at Stage 2. All those problems can be mitigated by using the elastic FWI, as the results obtained from Workflows 2 and 3 (Figures 5b, 5c, 5e and 5f). The comparison of reconstruction results between Workflow 2 and 3 shows that a similar V_p bias appears at the top edge of the gas cloud in the workflow only using the (V_p, V_s) parameterization, which further reveals the necessity of introducing (V_p, R) parameterization in the workflow and its validity in the complex model application.

CONCLUSIONS

In this study, we design the elastic FWI workflow for 4C ocean-bottom seismic data from the model parameterization point of view. By computing the radiation pattern of the partial derivative wavefields and deriving the FWI gradient expression, the data sensitivity and the model gradient feature are discussed for three different model parameterizations. Compared with the conventional (V_p, V_s) parameterization, the involving of S-related wave modes in (V_p, R) and (V_p, σ) parameterizations contribute to avoiding the misinterpretation of P-to-S-to-P converted waves into P-P reflected wave modes at the presence of strong elastic effects. The V_p gradient term in the R and σ gradient expressions can create binding and low-wavenumber compensation effects from V_p model building to stabilize the V_s reconstruction when there is a lack of reliable S-waves in the data. For the S-wave dominant data, like 3C geophone data, the less interparameter trade-off in the (V_p, V_s) parameterization makes the inversion focus on the V_s reconstruction. Those analyses lead us to design a two-step hierarchical elastic FWI workflow of first inverting hydrophone data with (V_p, V_p/V_s) parameterization and then 3C geophone data with (V_p, V_s) parameterization. Its robustness and reliability in the V_p and V_s joint reconstruction are verified by two numerical tests.

ACKNOWLEDGEMENTS

This study was partially funded by the SEISCOPE consortium (`http://seiscope2.osug.fr`), sponsored by AKERBP, CGG, CHEVRON, EQUINOR, EXXON-MOBIL, JGI, SHELL, SINOPEC, SISPROBE and TOTAL. This study was granted access to the HPC resources of CIMENT infrastructure (`https://ciment.ujf-grenoble.fr`), Cray Marketing Partner Network (`https://partners.cray.com`) and CINES/IDRIS/TGCC under the allocation 046091 made by GENCI.

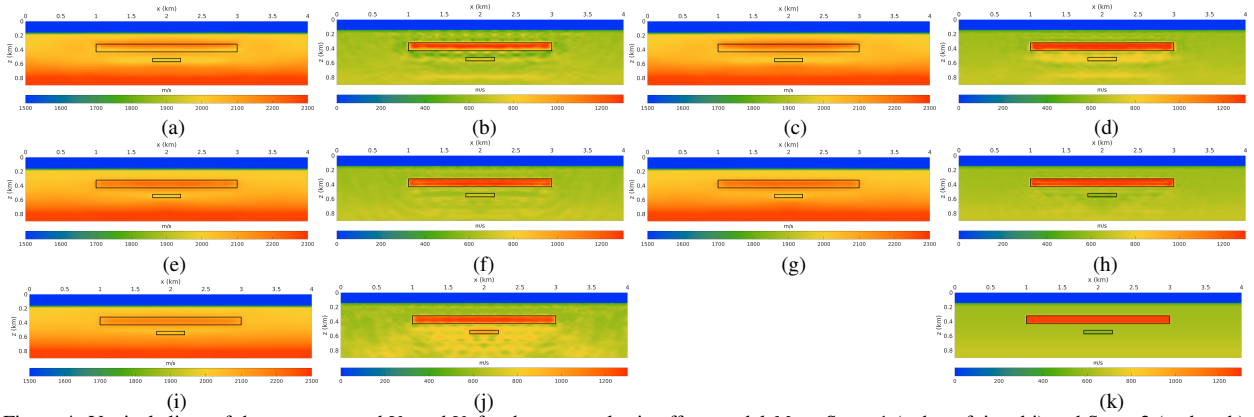

Figure 4: Vertical slices of the reconstructed V_p and V_s for the strong elastic-effect model M_5 at Stage 1 (a, b, e, f, i and j) and Stage 2 (c, d, g, h), and the true V_s model of M_5. From up to down, the inversion results correspond to parameterizations of (V_p, V_s), (V_p, R) and (V_p, σ), respectively. The black lines delineate the correct locations of the high-velocity overburden and low-velocity anomaly.

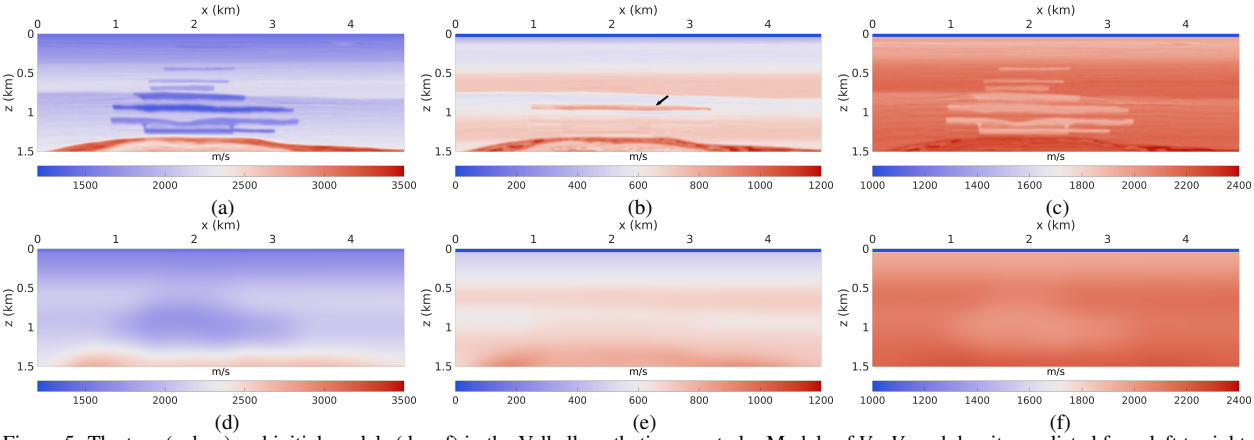

Figure 5: The true (a, b, c) and initial models (d, e, f) in the Valhall synthetic case study. Models of V_p, V_s and density are listed from left to right. The location of gas cloud with an extremely low Poisson's ratio ($\sigma = 0.125$) is indicated by the black arrow in (b).

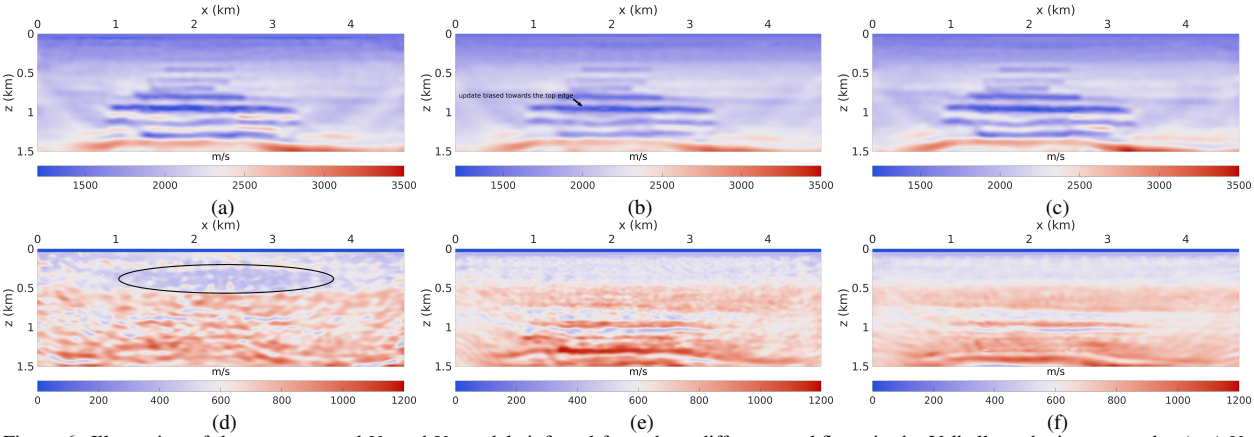

Figure 6: Illustration of the reconstructed V_p and V_s models inferred from three different workflows in the Valhall synthetic case study. (a-c) V_p models obtained at Stage 1, (d-e) V_s models obtained at Stage 2. Left: inversion results from Workflow 1, middle: inversion results from Workflow 2, and right: inversion results from Workflow 3.

REFERENCES

Agudo, Ò. C., N. V. da Silva, G. Stronge, and M. Warner, 2020, Mitigating elastic effects in marine 3-d full-waveform inversion: Geophysical Journal International, **220**, 2089–2104.

Barnes, C., and M. Charara, 2009, The domain of applicability of acoustic full-waveform inversion for marine seismic data: Geophysics, **74**, WCC91–WCC103.

Cao, J., R. Brossier, A. Górszczyk, L. Métivier, and J. Virieux, 2022, 3D multi-parameter full-waveform inversion for ocean-bottom seismic data using an efficient fluid-solid coupled spectral-element solver: Geophysical Journal International, **229**, 671–703.

Hamada, G., 2004, Reservoir fluids identification using vp/vs ratio?: Oil & Gas Science and Technology, **59**, 649–654.

Jain, P., C. Jambhekar, and P. Pandey, 2012, Identification of gas using vp/vs vis-a-vis poisson's ratio: 9th Biennial International Conference & Exposition on Petroleum Geophysics, 240.

Kamath, N., R. Brossier, L. Métivier, A. Pladys, and P. Yang, 2021, Multiparameter full-waveform inversion of 3D ocean-bottom cable data from the Valhall field: Geophysics, **86**, B15–B35.

Liu, E., X. Y. Li, and A. Chadwick, 2001, Multicomponent seismic monitoring of CO2 gas cloud in the utsira sand: a feasibility study: Saline aquifer CO2 storage phase 2 (SACS2): Work area 5 (Geophysics): feasibility of multicomponent seismic acquisition.

Morgan, J., M. Warner, R. Bell, J. Ashley, D. Barnes, R. Little, K. Roele, and C. Jones, 2013, Next-generation seismic experiments: wide-angle, multi-azimuth, three-dimensional, full-waveform inversion: Geophysical Journal International, **195**, 1657–1678.

Oh, J.-W., and D.-J. Min, 2017, Multi-parameter full waveform inversion using poisson's ratio for elastic media: Exploration Geophysics, **48**, 456–475.

Operto, S., R. Brossier, Y. Gholami, L. Métivier, V. Prieux, A. Ribodetti, and J. Virieux, 2013, A guided tour of multiparameter full waveform inversion for multicomponent data: from theory to practice: The Leading Edge, **Special section Full Waveform Inversion**, 1040–1054.

Operto, S., A. Miniussi, R. Brossier, L. Combe, L. Métivier, V. Monteiller, A. Ribodetti, and J. Virieux, 2015, Efficient 3-D frequency-domain mono-parameter full-waveform inversion of ocean-bottom cable data: application to Valhall in the visco-acoustic vertical transverse isotropic approximation: Geophysical Journal International, **202**, 1362–1391.

Plessix, R. E., 2006, A review of the adjoint-state method for computing the gradient of a functional with geophysical applications: Geophysical Journal International, **167**, 495–503.

Prieux, V., R. Brossier, S. Operto, and J. Virieux, 2013, Multiparameter full waveform inversion of multicomponent OBC data from valhall. Part 2: imaging compressional and shear-wave velocities: Geophysical Journal International, **194**, 1665–1681.

Sears, T. J., P. J. Barton, and S. C. Singh, 2010, Elastic full waveform inversion of multicomponent ocean-bottom cable seismic data: Application to alba field, u. k. north sea: Geophysics, **75**, R109–R119.

Sirgue, L., O. I. Barkved, J. Dellinger, J. Etgen, U. Albertin, and J. H. Kommedal, 2010, Full waveform inversion: the next leap forward in imaging at Valhall: First Break, **28**, 65–70.

Wang, H., O. Burtz, P. Routh, D. Wang, J. Violet, R. Lu, and S. Lazaratos, 2021, Anisotropic 3D elastic full-wavefield inversion to directly estimate elastic properties and its role in interpretation: The Leading Edge, **40**, 277–286.

Zong, J., S. Coskun, R. R. Stewart, N. Dyaur, and M. T. Myers, 2015, Salt densities and velocities with application to gulf of mexico salt domes: Presented at the SEG Annual Meeting Post-convention Workshop.